Plasma transferred arc surface alloying of Cr-Ni-Mo powders on compacted graphite iron

Feng, Jijun; Pan, Chunxu; Lu, Liulin; Huang, Qiwen; Cao, Huatang

Published in:
Journal of Iron and Steel Research International

DOI:
10.1016/S1006-706X(16)30096-6

Publication date:
2016

JOURNAL OF IRON AND STEEL RESEARCH, INTERNATIONAL. 2016, 23(6): 618-624

Plasma Transferred Arc Surface Alloying of Cr-Ni-Mo Powders on Compacted Graphite Iron

Ji-jun FENG[1,2], Chun-xu PAN[1], Liu-lin LU[2], Qi-wen HUANG[3], Hua-tang CAO[4]
(1. School of Physics and Technology, Wuhan University, Wuhan 430072, Hubei, China; 2. Dongfeng Commercial Vehicle Technology Center, Wuhan 430056, Hubei, China; 3. School of Materials Science and Engineering, Huazhong University of Science and Technology, Wuhan 430074, Hubei, China; 4. Department of Advanced Production Engineering, Engineering and Technology Institute Groningen, University of Groningen, Groningen 9747, The Netherlands)

Abstract: A Cr-Ni-Mo overlayer was deposited on the surface of compacted graphite iron (CGI) by the plasma transferred arc (PTA) alloying technique. The microstructure of Cr-Ni-Mo overlayer was characterized by optical microscopy (OM), scanning electron microscopy (SEM) equipped with energy dispersive spectroscopy (EDS), and X-ray diffractometer (XRD). Results show that the cross-section consists of four regions: alloying zone (AZ), molten zone (MZ), heat affected zone (HAZ), and the substrate (SUB). The microstructure of AZ mainly consists of cellular γ-(Fe,Ni) solid solution, residual austenite and a network of eutectic Cr_7C_3 carbide while the MZ area has a typical feature of white cast iron (M_3C-type cementite). The martensite/ledeburite double shells are observed in the HAZ. With decreasing the concentration of Cr-Ni-Mo alloys, the fracture mode changes from ductile in the AZ to brittle in the MZ. The maximum hardness of the AZ (450 $HV_{0.2}$) is lower than that of the MZ (800 $HV_{0.2}$). The eutectic M_3C and M_7C_3 carbides increase the microhardness, while the austenite decreases that of the AZ.
Key words: plasma transferred arc; compacted graphite iron; microhardness; fracture; Ni-Cr-Mo coating

Due to its high strength, low-cost, good thermal-fatigue resistance and excellent casting formability, compacted graphite iron (CGI) is a good candidate to produce complex castings with thin walls such as cylinders head, engine blocks, and brake disk[1,2]. However, low hardness and poor wear resistance of CGI limit its further industrial application. Currently, surface modification via high energy beams such as laser, electron beam, and plasma transferred arc (PTA) has been proved to be an effective method to increase the hardness, wear resistance and erosion resistance of parts exposed to severe service conditions. Such hardfacing can be achieved by adopting appropriate alloying elements such as chromium, nickel and molybdenum[3]. Although PTA has relatively lower energy density than laser and electron beam technique, PTA treatment has attracted increasing attentions in recent years because of its advantages of no requirement for any pre-treatment or a vacuum environment, high energy efficiency and low running costs[4-7]. During the PTA surface alloying process, the powders are encroached into a melting pool on the base material through plasma heating source. The powders thermal behavior such as melting, vaporizing and chemical reactions will produce hard alloy-carbides which are the carriers of improved properties like high hardness and good abrasion resistance[8].

However, a state of high residual stress and poor toughness usually appears inevitably during high-energy beam treatment process. For engine components served in the thermal, corrosive, and wearing service environments, ductile property should also be highly considered. To achieve a unique combination of these characteristics, rational alloys could be adopted to obtain the required microstructure and suitable mechanical properties within the hardfacing layer. The chromium carbides combined

Biography: Ji-jun FENG, Doctor Candidate, Professor; **E-mail**: fengjijun@dfcv.com.cn; **Received Date**: May 20, 2015
Corresponding Author: Chun-xu PAN, Doctor, Professor; **E-mail**: cxpan@whu.edu.cn

with nickel solid solution show a good surface finish, and reliable wear and corrosion resistances without heavily compromising the ductility under the condition of stress abrasion[9-11]. Although Ni-Cr systems are widely acknowledged as wear and corrosion protective coating, little attention has been paid to the formation of a Cr-Ni-Mo overlayer on the surface of CGI by the PTA technique. Thus, in this paper, PTA was used as the heat source to produce a Cr-Ni-Mo overlayer on the CGI. The microstructure, phases, fracture and microhardness of the PTA modified layer were studied.

1 Experimental Procedure

The starting microstructure of CGI(RuT350) consists of vermicular graphites and ferrites surrounded by island-like pearlites and its chemical composition is shown in Table 1.

Table 1 Chemical composition of CGI (RuT350) mass%

C	Si	S	Mn	P	Mg	RE	Fe
3.60	2.60	0.01	0.53	0.04	0.01	0.02	Balance

The specimens were in the form of plate with length of 60 mm, width of 30 mm and thickness of 15 mm. The specimens were polished by 300 grit emery paper and then cleansed via acetone to remove oxides and residue. The alloying powders were mainly composed of Ni, Cr, Mo, and Cu, as shown in Table 2.

Table 2 Chemical composition of Cr-Ni-Mo coating mass%

Ni	Cr	Mo	Cu
50—65	20—25	20	10—15

The powders mixed with moderate amount of sodium silicate were then brushed on the surface of substrate. The equipment of PTA can achieve a maximum energy level of 10^6 W/cm^2[12]. Fig. 1 depicts the schematic diagram of the PTA torch. A plasma arc is generated between the tungsten needle and the specimen, where the sample serves as the anode and the tungsten needle serves as the cathode. Argon was employed as both the plasma source gas and shielding gas during the PTA-alloying process. The main experimental parameters of the PTA alloying process are listed in Table 3.

Transverse sections of PTA Cr-Ni-Mo alloying on CGI were obtained by parallel cutting to the length direction. The sample was prepared by mounting, grinding, polishing and then etched with 4 vol.% nital or chloroazotic acid. Microstructure and element distribution of the sample were examined by SU-70 scanning electron microscopy (SEM) equipped with Oxford energy dispersive X-ray spectroscope (EDS). The X-ray diffractometer (XRD) using CuKα (λ = 1.5403×10^{-4} μm) radiation was applied to identify the phases of the built-up layer. And microhardness of the cross-section along the depth of PTA-modified layer was determined by Vickers microhardness tester (EVERONE MH-6). Fracture tests were also conducted to discuss the failure modes of the PTA Cr-Ni-Mo hardfacing overlayer.

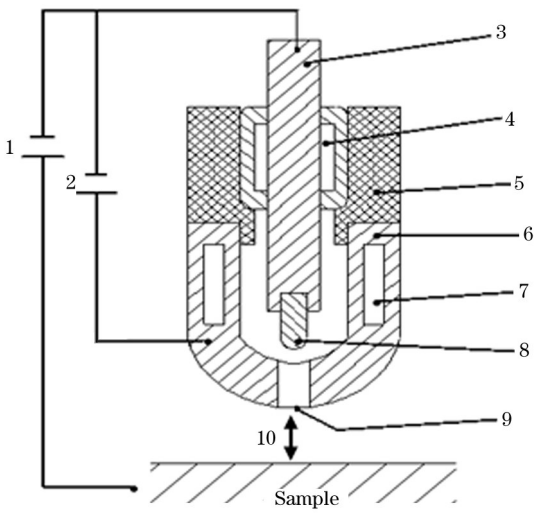

1—Plasma power source; 2—Pilot power source; 3—Popper electrode; 4—Cooling water for electrode; 5—Insulating bush; 6—Nozzle; 7—Cooling water for nozzle; 8—Tungsten needle; 9—Nozzle tip; 10—Work distance.

Fig. 1 Schematic diagram of the PTA torch

Table 3 Parameters of the PTA surface alloying

Main arc/A	Traveling speed/(mm·min^{-1})	Diameter of nozzle/mm	Working distance/mm
90	800	4	2

2 Results and Discussion

2.1 Microstructure

The macroscopic appearance of PTA alloying on the CGI sample is illustrated in Fig. 2(a), which exhibits smooth surface without remarkable porosities and cracks. The cross-section morphology of the alloying layer is illustrated in Fig. 2(b), and the arrow shows the PTA modified depth from the surface to the substrate (SUB). It is noticeable that the microstructural feature of the overlayer can be divided into

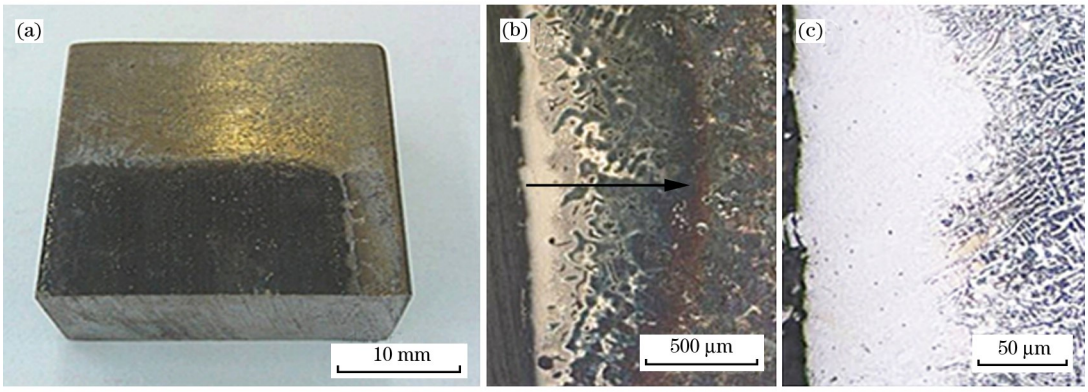

(a) Macrograph; (b) Low-magnified cross-section morphology; (c) Microstructural evolution from AZ to MZ.

Fig. 2 Observation of the PTA alloyed layer on the CGI sample

four parts by three obvious boundaries: alloying zone (AZ), molten zone (MZ), heat affected zone (HAZ) and the SUB. Due to the Gaussian distribution of energy[13], the overlayer has a metallurgical bond with the matrix by forming a moon-like molten pool. The thickness of the overlayer is approximately 0.25 mm. According to Fig. 2(c), the upper AZ obviously presents bright white, implying a high enrichment distribution of alloying carbides as well as a good resistance against the nital's corrosion. The comparatively uniform overlayer could be obtained by multiple overlapping process (overlapping rate=25%).

Fig. 3 shows the microstructural feature of PTA alloyed overlayer. It is evident from Figs. 3(a) and 3(b) that the graphite in the AZ melts almost completely and is no longer formed again during resolidi-

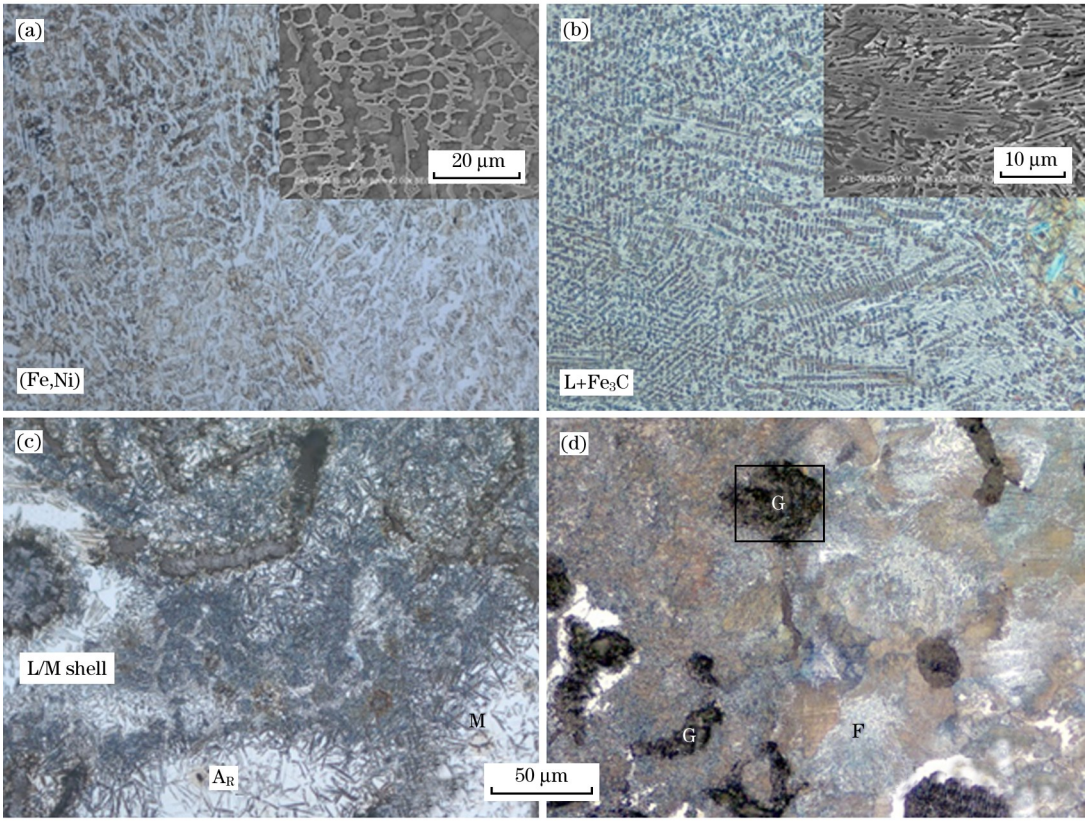

L—Ledeburite; M—Martensite; A_R—Retained austenite; G—Graphite; P—Pearlite; F—Ferrite.
(a) AZ (the inset is the SEM image showing cellular structure); (b) MZ (the inset is SEM image showing the bulky Fe_3C); (c) HAZ; (d) SUB.

Fig. 3 Microstructural evolution after PTA surface alloying

fication. This is because PTA treatment is a rapid non-equilibrium solidification and the rapid self-quenching after PTA alloying suppresses the reformation of graphite in favor of the formation of white cast iron (cementite)[14]. From the Fe-Ni binary phase diagram[15], Fe and Ni firstly form a reticular γ-(Fe, Ni) solid solution under the liquidus line. During the melting and solidification, pre-placed Ni by PTA generally cannot produce chemical reactions with other elements such as Cr, Mo and C, so it plays a key role in forming γ-(Fe,Ni) solid solution with Fe in the substrate, which is also confirmed by XRD analysis, as shown in Fig. 4. In spite of this, Ni is a strong element to facilitate the formation of austenite, and this can be part of reasons for the existence of large amount of residual austenite ($CFe_{15.1}$) in the AZ. Another reason for the retention of austenite is the high amount of alloying elements in the AZ which lowers the onset transformation temperature of austenite to martensite at room temperature, and there is no enough time for the austenite to completely change into martensite in the rapid resolidification. The complex phase Cr_7C_3 is formed in the alloy as re-precipitated carbides during the fast cooling process. Finally, at the eutectic point, remaining liquids solidify into a network of eutectic cementite (Fe_3C)[16]. Hence, the microstructure of AZ mainly consists of γ-(Fe, Ni) solid solution, residual austenite and a network of eutectic Cr_7C_3 carbide and Fe_3C-type cementite. With increasing the distance from the surface, the temperature gradient decreases rapidly, which hinders the diffusion of alloying elements and thus limits the depth of the alloyed layer. The microstructure in the MZ is chiefly composed of a network of eutectic Fe_3C and ledeburite as shown in Fig. 3(b), which is a typical characteristic of white cast iron. These dendrites are characterized by long primary and secondary arms, indicating that there is an extremely high cooling rate during solidification. Fig. 3(b) also shows that the needle-like martensite is located in the transformed retained austenite cells in the transition zones between the MZ and HAZ, indicating that the transformed austenite partly evolves into martensite and is partly retained after solidification[3]. The HAZ microstructure is mainly composed of needle-like martensite with some un-melted graphites owing to the decreased plasma energy with the proofs of the existence of martensite and ledeburite double shells as shown in Fig. 3(c). With the increase of distance from the HAZ to the SUB, the fraction of martensite decreases whereas the fraction of pearlite substantially increases until rising up to the original level as the SUB. It should be noted that the presence of Mo carbides was not directly confirmed by the XRD results.

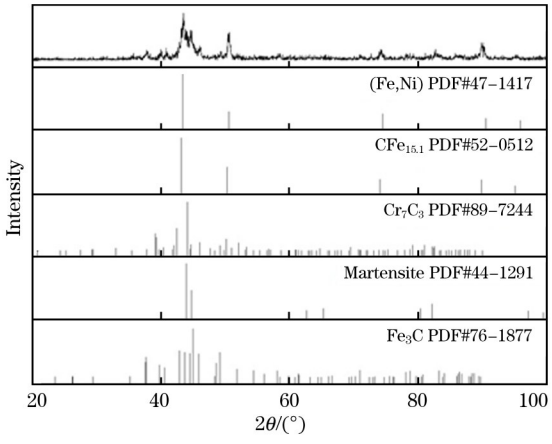

Fig. 4 X-ray diffraction pattern of the PTA-alloyed surface layer

Fig. 5 shows the energy dispersive spectrum of the overlayer, which discloses the chemical composition gradient of Cr, Ni, Mo, and Cu present in the alloying overlayer. In the area from surface to the depth of 0.15 mm (approximately equal to the thickness of the alloying zone), it is clearly seen that the contents of Ni, Cr, and Mo show a gradual decrease from the AZ to the MZ while the Cu concentration does not change significantly. This provides a proof for the formation of a functionally graded surface where the alloying elements are tapered gradually along the depth direction. Meanwhile, the content of Fe shows an opposite trend, rebounding from the minimum in the near surface to the original content of the as-received CGI, which further confirms that the alloying materials have been metallurgically bonded with the CGI substrate. It should be noted that owing to energy degradation along the depth

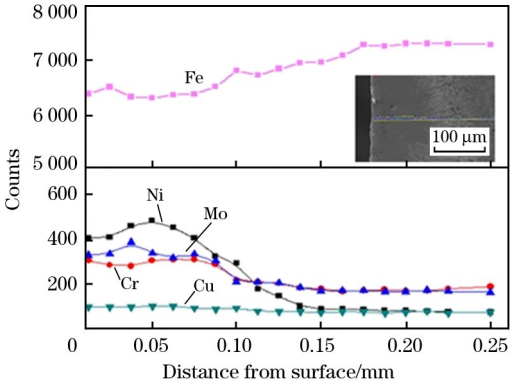

Fig. 5 Elemental distribution along the PTA-modified layer

after the PTA torch moving away, the alloying elements are unable to diffuse continually during the subsequent cooling; thus, only a limited thickness of alloying overlayer is formed at the near-surface. Fig. 6 shows the surface scanning microanalysis of the middle region of alloyed zone. The backscattered electron (BSE) image presented in Fig. 6(a) shows the network morphology of eutectic carbides. The degree of light contrast in Figs. 6(b)—6(f) represents the relative concentrations of corresponding elements, respectively. From Figs. 6(c), 6(d) and 6(f), it can be evidently found that the elements of Cr, Mo, and C are enriched in the bar-shaped structure or among the grain boundaries, while on the contrary, the same areas are deficient in Fe. This could effectively confirm the formation of Cr and Mo carbides. Meanwhile, the bulk-like particles or the intracrystallines shown in Fig. 6(e) are assumed to be Ni-rich solid solution.

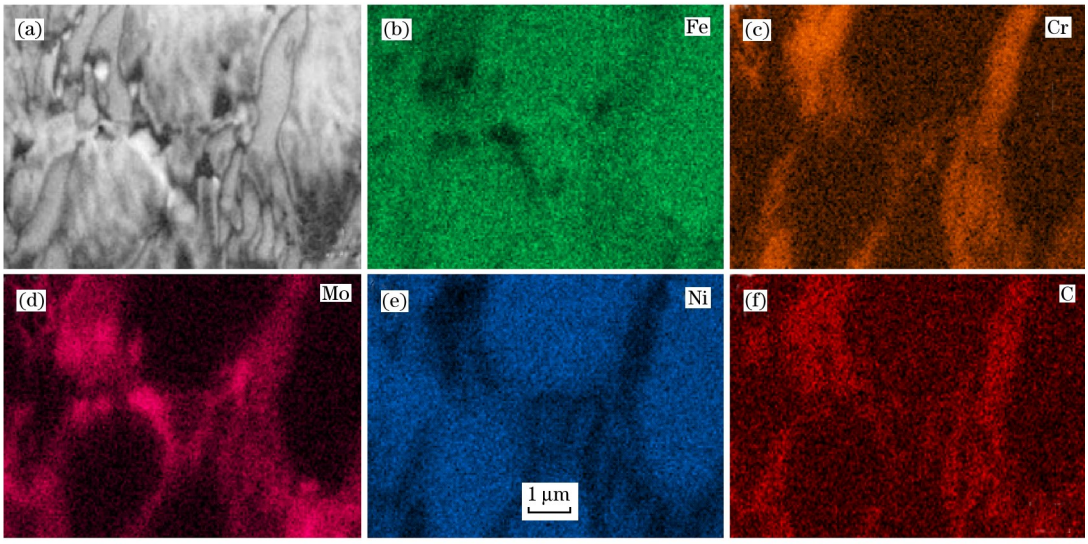

Fig. 6 EDS mapping of the middle region of alloying zone

2.2 Fracture analysis

The SEM micrographs of the tensile fracture of PTA-alloyed overlayer are shown in Fig. 7. It can be seen that the fracture mode at the AZ is predominately ductile, because a great number of dimples and tearing ridges connecting the microscopic dimples are observed in Figs. 7(b) and 7(c). This is because the γ-(Fe, Ni) and austenite at the AZ are ductile phases, which contribute to the ductile fracture features. At the MZ, the large eutectic dendrites, martensite and blocky cementite are brittle, which render cracks to spread along the interface of the eutectics, presenting typical river patterns and intergranular fractures (Fig. 7(d)). Therefore, the fracture mode almost changes to be fully brittle. At the HAZ, the main characteristic of the fracture is still a bit brittle due to its intergranular and quasi-cleavage fracture, as shown in Figs. 7(f)—7(h). The SUB, however, presents obvious cleavage steps but still seems more ductile than the brittle MZ thanks to the relatively good toughness of CGI. Therefore, it can be safely concluded that the AZ shows the best plastic capability in the cross-section, indicating that the Cr-Ni-Mo overlayer could improve the ductile property of CGI.

2.3 Microhardness profile

The microhardness profile as a function of distance from the surface is shown in Fig. 8. According to the microstructure analysis, four regions with different ranges of microhardness value could be distinguished. It could be clearly seen that the maximum microhardness (about 800 $HV_{0.2}$) is obtained in the MZ rather than the top surface of AZ (approximately 450 $HV_{0.2}$). The microhardness decreases gradually with an extending depth of approximately 1 mm and levels off at approximately 270 $HV_{0.2}$, which is the original microhardness of the substrate. The microhardness of the PTA-alloyed sample is approximately 1.5—3.0 times that of the untreated substrate, proving that PTA alloying process can enhance the microhardness of substrate effectively. This significant increase in hardness is mostly related to the phase transformations. On one hand, the eutectic carbides Cr_7C_3 and M_3C formed at the AZ contribute to the hardness increase; on the other hand, the γ-(Fe, Ni) and austenite $CFe_{15.1}$ at the AZ lead to the hardness reduction. From the HAZ to the

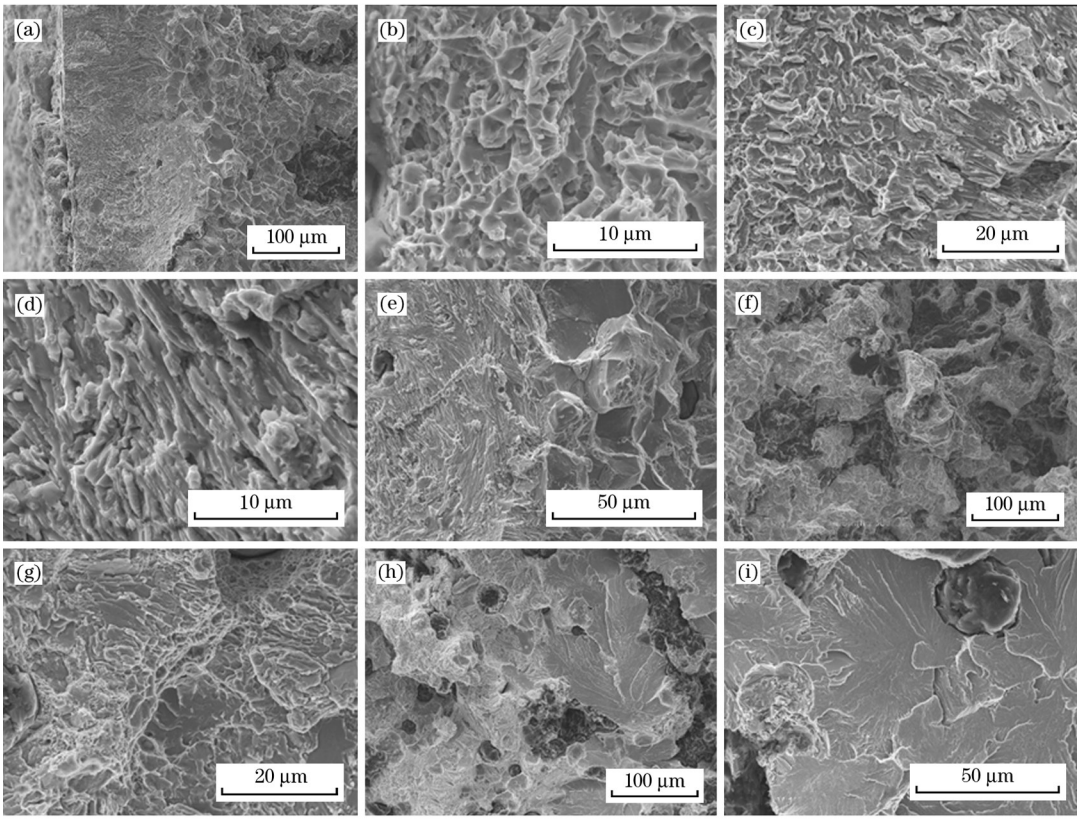

(a) Overview of AZ to MZ; (b) Magnified AZ zone; (c) Transition between AZ and MZ zone; (d) Magnified MZ zone; (e) Transition between MZ and HAZ (intergranular zone); (f) HAZ (from intergranular zone to quasi-cleavage); (g) Magnified HAZ (quasi-cleavage zone); (h) Transition between HAZ (quasi-cleavage zone) and SUB; (i) Magnified SUB (cleavage zone).

Fig. 7 Fractography of the PTA-alloyed overlayer from outer surface to inner substrate

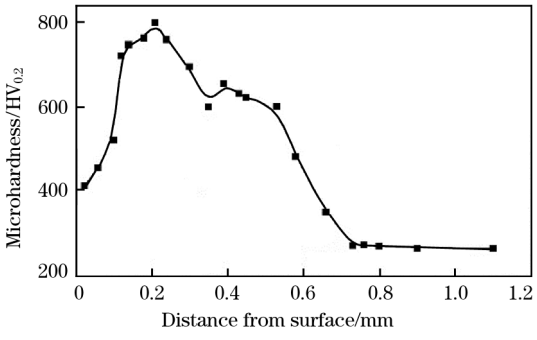

Fig. 8 Microhardness profile along the depth of the PTA-alloyed layer

SUB, the microhardness shows a gradual decrease. This is because the volume fraction of martensite and cementite phases reduces as a result of declining cooling rate with increasing the distance from surface.

Notably, the abrupt discontinuity in the hardness is considered as one of the key reasons for poor adhesion, leading to exfoliation and splitting of coating. Thus, the slight gradient in the microstructure variation along the depth of the PTA-alloyed layer contributes to good adhesion to the matrix, which cannot be produced by conventional processing technique. It is acknowledged that the hardened layer at the surface could protect the matrix from wear but at the expense of some toughness. However, in this coating system, due to the formation of rich γ-(Fe, Ni) and the good ductility of austenite, the modified surface still keeps a good ductile profile though sacrificing some microhardness.

3 Conclusions

The PTA strengthening technique successfully produces a Fe-C-Cr-Ni-Mo alloying zone on the surface of compacted graphite iron. The cross-section after PTA alloying could be divided into four regions: AZ, MZ, HAZ and SUB. The content distribution of Cr, Ni, and Mo decreases gradually from AZ to HAZ while that of Fe shows an upward trend, indicating that a reliable metallurgical bond was achieved between the hardfacing overlayer and the SUB. The microstructure of AZ shows that it contains γ-(Fe, Ni), austenite coupled with a network of eutectic Cr_7C_3 carbide and Fe_3C cementite, which was also confirmed by the XRD technique.

The maximum microhardness is determined in the subsurface of PTA overlayer with a value of about 800 $HV_{0.2}$, which is approximately 1.5—3.0 times that of the matrix. For the fracture morphology of the AZ cross-section, a large number of dimples and tearing ridges connecting the microscopic dimples are observed and the fracture surface shows mixed intergranular fracture and river pattern morphology in the MZ. The favorable increase in microhardness at no sacrifice of good ductility in the AZ is attributed to the generation of γ-(Fe, Ni), austenite and the network of eutectic Cr_7C_3 carbide as well as grain refining induced by the fast non-equilibrium solidification.

References:

[1] Z. Jing, H. Zhou, P. Zhang, C. Wang, C. Meng, D. Cong, Appl. Surf. Sci. 271 (2013) 329-336.
[2] T. Slatter, R. Lewis, A. H. Jones, Wear 270 (2011) 302-311.
[3] A. Amirsadeghi, M. H. Sohi, S. F. K. Bozorg, J. Iron Steel Res. Int. 15 (2008) No. 4, 86-94.
[4] H. T. Cao, X. P. Dong, Q. W. Huang, Z. Pan, J. J. Li, Z. T. Fan, Int. J. Miner. Metall. Mater. 21 (2014) 363-370.
[5] F. Y. Hung, Z. Y. Yan, L. H. Chen, T. S. Lui, Surf. Coat. Technol. 200 (2006) 6881-6887.
[6] H. Deng, H. Shi, S. Tsuruoka, Surf. Coat. Technol. 204 (2010) 3927-3934.
[7] V. Balasubramanian, A. K. Lakshminarayanan, R. Varahamoorthy, S. Babu, J. Iron Steel Res. Int. 16 (2009) No. 1, 44-53.
[8] H. T. Cao, X. P. Dong, Q. W. Huang, Z. Pan, J. J. Li, Z. T. Fan, Adv. Mater. Res. 852 (2014) 188-192.
[9] A. Zikin, I. Hussainova, C. Katsich, E. Badisch, C. Tomastik, Surf. Coat. Technol. 206 (2012) 4270-4278.
[10] J. H. Chang, C. P. Chang, J. M. Chou, R. I. Hsieh, J. L. Lee, Surf. Coat. Technol. 204 (2010) 3173-3181.
[11] Z. Huang, Q. Hou, P. Wang, Surf. Coat. Technol. 202 (2008) 2993-2999.
[12] Q. W. Huang, S. B. Hu, A. H. Wang, Heat Treatment of Materials 36 (2011) 1-8.
[13] J. Grum, R. Šturm, J. Mater. Process. Technol. 147 (2004) 351-358.
[14] J. H. Abboud, Mater. Des. 35 (2012) 677-684.
[15] Q. Wu, W. Li, N. Zhong, W. Gang, W. Haishan, Mater. Des. 49 (2013) 10-18.
[16] M. Shamanian, S. M. R. M. Abarghouie, S. R. M. Pour, Mater. Des. 31 (2010) 2760-2766.